Chemical Engineering Journal 493 (2024) 152608

Contents lists available at ScienceDirect

Chemical Engineering Journal

journal homepage: www.elsevier.com/locate/cej

Molecular engineering of a MOF with an ionic liquid sheath for direct air separation at ambient conditions

Ozce Durak [a,b], Nitasha Habib [a,b], Hasan Can Gulbalkan [a,b], Ahmet Safa Aydogdu [a,b], Ray Ozdemir [c], Seda Keskin [a,b,*], Alper Uzun [a,b,d,*]

[a] Department of Chemical and Biological Engineering Koç University, Rumelifeneri Yolu, 34450 Sariyer, Istanbul, Turkey
[b] Koç University TÜPRAŞ Energy Center (KUTEM), Koç University, Rumelifeneri Yolu, 34450 Sariyer, Istanbul, Turkey
[c] Framergy, Inc. 800 Raymond Stotzer Parkway 2011A College Station TX 77845 USA
[d] Koç University Surface Science and Technology Center (KUYTAM), Koç University, Rumelifeneri Yolu, 34450 Sariyer, Istanbul, Turkey

ARTICLE INFO

Keywords:
Adsorption
Air Separation
Metal-organic Framework
Ionic Liquid

ABSTRACT

Combining ionic liquids (ILs) with metal–organic frameworks (MOFs) offers broad prospects for gas separation applications. However, identifying the best IL-MOF pair for a target gas separation solely based on experimental techniques is impractical. Herein, the promising IL and MOF combination was selected among 35,672 distinct ILs and 5,629 different MOFs by fusing computational methods at different molecular scales, density functional theory, conductor-like screening model for real solvents calculations, and grand canonical Monte Carlo simulations to engineer a MOF with an IL sheath (MOFILS) for direct air separation. The new MOFILS composed of $[P_{6,6,6,14}][DCA]$ and PCN-250(Fe) designed at the atomic level was then experimentally synthesized after fine-tuning the MOF to achieve high-performance air separation. An exceptionally high ideal O_2/N_2 selectivity of 26 was reached at 1 bar and 25 °C, boosting the benchmark value by four-times. The results of equilibrium and dynamic gas adsorption measurements further indicated a remarkably high selectivity of 382 for the separation of O_2/N_2:21/79 mixture, demonstrating the broad potential of the MOFILS designed in this work for direct air separation.

1. Introduction

Separation of high-purity oxygen (>99%) from air holds extreme importance for both medical (oxygen therapy [1], mechanical ventilation [2]) and industrial (oxygen-enriched combustion [3], fuel cells [4], gas conversion [5]) purposes. Hence the discovery of O_2-selective adsorbents is of vital importance. Among various other needs, providing high-purity O_2 has become especially essential for medical applications during the COVID-19 outbreak due to the rising symptoms, such as shortness of breath, which requires the patient to be put on oxygen support [6]. According to World Health Organization (WHO) statistics, about 15% of COVID-19 patients with severe illness needed oxygen support via mechanical ventilation or oxygen therapy [7,8]. In this regard, on-site purification of oxygen from air has gained attention by eliminating the need for transportation. Oxygen concentrators utilize pressure-swing adsorption (PSA) technology to obtain purified oxygen from air with more than 90% concentration. However, current PSA technologies lack cost-effective and highly selective adsorbent materials. Conventional adsorbents, such as cation-exchange zeolites 5A (CaA) and 13X (NaX), are generally N_2-selective and require frequent regeneration cycles because of the high N_2 (>78 vol%) concentration in the air [9]. Yet, the rational design of O_2-selective adsorbents for obtaining O_2 from air, O_2/N_2 separation, possesses a significant challenge due to the similar physical and chemical properties of these molecules, such as kinetic diameters (O_2: 3.46 Å, N_2: 3.64 Å), quadrupole moments, and polarizabilities [10].

In the last decade, metal–organic frameworks (MOFs) have emerged as a promising class of porous materials, and several studies reported their potential for O_2/N_2 separation [11,12]. Particularly, MOFs having coordinatively unsaturated (open) metal sites are the subject of interest because their redox-active metal centers provide open binding sites for O_2. Tunability of organic and inorganic constituents of MOFs offers opportunities for engineered O_2-selective adsorbents having the desired redox-active binding sites. There are various efforts in this direction to design O_2-selective MOFs, such as $Cr_3(BTC)_2$ [13], Cr-BTT [14], Co-BTTri [15], Co-BDTriP [15], Fe-BTTri [16], and MOF-177 [17].

* Corresponding authors.
E-mail addresses: skeskin@ku.edu.tr (S. Keskin), auzun@ku.edu.tr (A. Uzun).

https://doi.org/10.1016/j.cej.2024.152608
Received 29 February 2024; Received in revised form 24 April 2024; Accepted 26 May 2024
Available online 27 May 2024
1385-8947/© 2024 The Authors. Published by Elsevier B.V. This is an open access article under the CC BY license (http://creativecommons.org/licenses/by/4.0/).

Although most of these MOFs offer good performance at cryogenic temperatures, as given in Table S1 of Supporting Information (SI), their O_2/N_2 selectivity significantly decreases at room temperature [16,18]. Thus, there is a strong need for the rational design of structurally stable, efficient, and high-performance O_2-selective materials at ambient conditions.

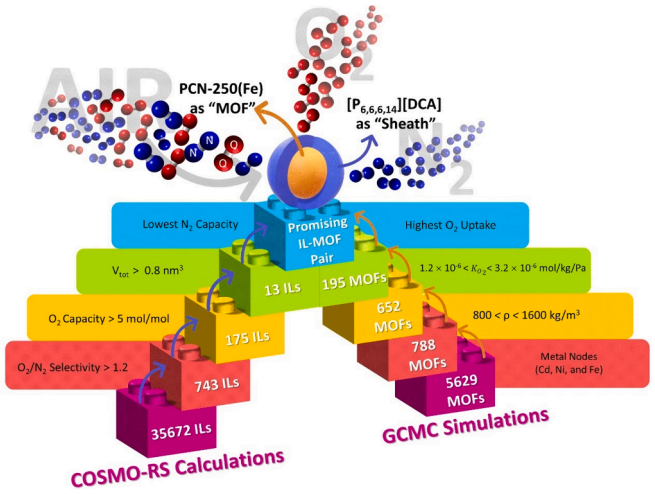
Within this scope, post-synthetic modification of MOFs with ionic liquids (ILs) has become one of the most prominent methods among various techniques considering its facile application allowing direct control over molecular affinity with the task-specific selection of ILs [19,20]. Numerous studies reported significantly improved selectivities for different gas separations upon post-synthetic modification of MOFs with ILs [21–23]. Therefore, this technique can potentially be employed to design highly O_2-selective MOFs with the rigorous determination of the proper IL and MOF combination. One drawback of this approach is that when the IL molecules are incorporated inside the MOF cages, they reduce the available pore volume, negatively impacting the gas uptakes. When the IL is deposited on the external surface area of the MOF, on the other hand, the resulting structure eliminates this problem and provides improved selectivities because of the presence of the IL sheath, which acts as a selective filter controlling the passage of the gas molecules into the MOF's cages [24]. Hence, the rational design of such a *MOF with an IL sheath* (MOFILS) that can achieve superior O_2 selectivity without sacrificing the O_2 uptake offers a broad prospect for direct air separation. However, because the number of different IL-MOF combinations that can be obtained by combining ILs with MOFs is almost infinite [25], it is not possible to investigate all of the possible MOFILS based solely on experimental techniques.

In this work, we proposed a hierarchical methodology combining computational tools with experiments to design a MOFILS offering an exceptional O_2/N_2 separation performance at ambient conditions. First, 35,672 different ILs were screened by using the Conductor-like Screening Model for Realistic Solvents (COSMO-RS) to select an IL with high O_2 affinity. Density functional theory (DFT) calculations were then performed to investigate the quantitative interactions between the selected IL, trihexyltetradecylphosphonium dicyanamide, [$P_{6,6,6,14}$][DCA], and the gas molecules, O_2 and N_2. PCN-250(Fe) was chosen among 5629 different types of MOFs because of its high O_2 uptake based on grand canonical Monte Carlo (GCMC) simulation results, commercial availability, scalability, and robustness. The new MOFILS, [$P_{6,6,6,14}$][DCA]/PCN-250(Fe), was then synthesized and characterized in detail. O_2 and N_2 adsorption measurements demonstrated that this MOFILS offers an exceptional O_2 separation performance over N_2 even at atmospheric pressure and room temperature without the loss of O_2 capacity for at least ten adsorption-regeneration cycles. Our results illustrate the first example of fusing quantum chemical calculations, molecular simulations, and experiments for engineering a novel adsorbent material through facile post-synthetic techniques for efficient direct O_2 separation from air at ambient conditions.

2. Methodology for the rational design of O_2 selective MOFILS

2.1. IL selection

The proposed hierarchical approach to select the best-performing MOFILS is presented in Scheme 1. First, the O_2 and N_2 activity coefficients of a large set of 35,672 ILs consisting of 364 cations and 98 anions were estimated by performing COSMO-RS calculations using COSMOThermX version C30_1602 (COSMOlogic GmbH & Co KG, Germany). A wide range of IL families was considered including imidazolium-, phosphonium-, ammonium-, pyridinium-, pyrrolidinium-, piperidinium-, quinolium-, guanidinium-, sulfonium-, morpholinium-, thiazolium-, pyrazolium-, choline-, nicotinic acid-, thiophenium-, bicyclo-, isouronium-, and isothionium-based ones. The resulting database with the estimated capacities of O_2 and N_2 in each of these ILs, and their O_2/N_2 selectivities along with the optimized geometries of [$P_{6,6,6,14}$][DCA] structures are publicly provided (https://github.com/hasancangulbalkan/ILMOF_directairseparation.git). In this regard, having a high solvent capacity (C_i^{∞}) and selectivity ($S_{i/j}$) is strongly desired for effective gas separation [26]. Moreover, having a high molecular volume is also important to obtain a MOFILS structure, where IL is deposited on the external surface of the MOF particle without occupying any space inside the internal pore volume. Hence, the following criteria were set to screen ILs: (i) O_2/N_2 selectivity $\left(S_{O_2/N_2}\right) > 1.2$, which decreased the number of ILs from 35,672 to 743; (ii) O_2 capacity $\left(C_{O_2}^{\infty}\right) > 5$ mol/mol, further reducing the number of ILs to 175; (iii) molecular volume > 0.8 nm^3/molecule leading to an additional reduction in the number of IL candidates to 13. Among the remaining 13 ILs, [$P_{6,6,6,14}$][DCA] was identified as the most promising IL since it offers the lowest $C_{N_2}^{\infty}$.



Scheme 1. The proposed hierarchical approach for selecting the most promising IL and MOF pair to achieve superior O_2/N_2 separation performance.

Next, the DFT calculations were performed to confirm the high O_2 affinity of the selected IL. The most stable IL conformer was identified by considering a variety of cation–anion combinations that represent [$P_{6,6,6,14}$][DCA]. Figure S1 demonstrates three conformer geometries with the lowest equilibrium energy. The equilibrium energy of Conformer 1 was 5.17 and 16.39 kJ/mol lower than that of Conformer 2 and Conformer 3, respectively. Hence, Conformer 1 was used to carry out the rest of the investigation to determine how the gas molecules interact with [$P_{6,6,6,14}$][DCA]. The geometry optimization calculations, performed using IL and gas molecules together, indicated different interactions with the IL, as presented in Figure S2. The IL's anion and cation are both near O_2. As a Lewis base, O_2 donates its lone pair electrons to Lewis acidic positively charged C ($q_c = 0.464e$) of [DCA] $^-$ and forms a strong Lewis acid-base type interaction with the corresponding C···O1 and C···O2 distances of 2.66 and 2.71 Å, respectively. The hydrogens of the cation additionally stabilize O_2 molecules by forming H-bonds. In contrast, the atoms of N_2 molecule form weak hydrogen bonds with the cations' hydrogen atoms on the hexyl chain. As a result, O_2 shows a significantly higher affinity towards [$P_{6,6,6,14}$][DCA] with a calculated binding energy of 30.1 kJ/mol compared to that of N_2, 8.1 kJ/mol. Besides these DFT calculations, the effect of pressure on O_2 and N_2 solubilities in IL was examined by COSMO-RS calculations between 0.001–1 bar at 25 °C. Figure S3 demonstrates that O_2 has significantly higher solubility in [$P_{6,6,6,14}$][DCA] than N_2 at 25 °C and pressures that we examined.

2.2. MOF selection

We used the CoRE MOF database [27], which contains 5629 distinct

MOFs and O_2 adsorption data from our previous work [28], to identify a promising MOF for O_2 adsorption at 1 bar and 298 K, as shown in Scheme 1. MOFs were first screened based on several structural and chemical properties, which have been demonstrated as the most important MOF descriptors for high-performance O_2/N_2 separation by recent machine learning studies [29,30]: (i) metal type (transition metals: Cd, Ni, and Fe are the optimal ones), (ii) density (ρ) (between 800–1600 kg/m^3), and (iii) Henry's constant of O_2 (K_{O_2}) (between 1.2×10^{-6}-3.2×10^{-6} mol/kg/Pa). As a result of this screening, the most promising MOF was identified as PCN-250(Fe) for further experimental investigation as it offers the highest O_2 uptake in addition to being robust and commercially available through reliable vendors [31].

3. Methods

3.1. Computational method

COSMOthermX (C30_160) software was used to perform COSMO-RS calculations. COSMO-RS is a widely utilized computational modeling tool for qualitatively estimating the solubilities of different gases in bulk ILs [32,33]. The TZVPD-FINE parameterizations were used to obtain the solvent capacity $\left(C_{ij}^{\infty}\right)$ of the bulk $[P_{6,6,6,14}][DCA]$ for O_2 and N_2 at infinite dilution conditions. The vapor pressure of the pure component i $\left(P_i^{vap}\right)$ was divided by solvent capacity $\left(C_{ij}^{\infty}\right)$ to determine the Henry's constant (K_i). K_{O_2} and K_{N_2} values were computed at 25 °C for 35,672 ILs (combinations of 364 cations and 98 anions).

The pore limiting diameter (PLD) and the largest cavity diameter (LCD) of activated and non-activated pristine PCN-250(Fe) were calculated using Zeo++ software [34]. DFT calculations were performed to quantitatively investigate the interactions of O_2 and N_2 with $[P_{6,6,6,14}][DCA]$. The Gaussian09 software package was used to find every potential conformation of the molecules by employing the Becke-three-parameter-Lee-Yang-Parr (B3LYP) functional, Grimme's D2 correction and the 6-31G(d) basis set [35–37]. The vibrational frequency analysis was used to ensure that the global minimum geometries were obtained and that no imaginary frequencies were left on the optimized geometries. The 6-31G(d) basis set and single point calculations on the optimized geometries were used to compute the binding energies between the gases and the IL molecule, as well as Natural Bond Orbital (NBO) atomic charges. The nature of the electrostatic interactions between the IL and the gases was investigated using NBO analyses [38]. The binding energies between the adsorbed gases and the IL are computed by using $\Delta E_{bind} = E_{A+B} - (E_A + E_B) + \delta^{BSSE}$ where E_{A+B} is the energy of the system consisting of the adsorbed gas molecule (O_2 or N_2) and $[P_{6,6,6,14}][DCA]$, E_A is the energy of $[P_{6,6,6,14}][DCA]$, E_B is the energy of the gas molecule, and δ^{BSSE} is the basis set superposition error correction employed by Counter Poise approach [39,40].

3.2. Experimental materials and method

The PCN-250(Fe) was kindly provided by Framergy, and $[P_{6,6,6,14}][DCA]$ was purchased from Iolitec (>98%), respectively. The acetone used for the synthesis of the MOFILS (reagent grade, >99.5%) was purchased from Sigma-Aldrich. PCN-250(Fe) and $[P_{6,6,6,14}][DCA]$ were stored in an Ar-filled MBraun glovebox. Gasses, He (>99.9 vol%), N_2 (>99.9 vol%), and O_2 (>99.5 vol%), used in synthesis and gas sorption studies, were purchased from Air Liquide.

Different concepts of adsorbent-absorbent approaches have been reported in the literature, such as IL/MOF composites and porous liquids (PLs) [41,42]. The PLs are characterized by the excess amount of absorbent liquid, which is mixed with porous adsorbent, creating a PL suspension with an enhanced sorption capacity [43]. On the other hand, the IL/MOF composites are characterized in their powder form as a limited amount of absorbent liquid is used with adsorbent. The powder state sorbents have significant advantages over liquid sorbents thanks to the ease of processing and utilization, hence maintaining the powder form is crucial. Therefore, to maintain the powdered state, the optimum IL loading of MOFILS is determined as the highest IL loading before reaching the wetness limit (45 wt.%), as the ideal O_2/N_2 selectivity of the synthesized MOFILS increases with the increasing loading of $[P_{6,6,6,14}][DCA]$ as demonstrated in Table S2. As-received PCN-250(Fe) was first heat-treated at 240 °C for 12 h in a Quantachrome XeriPrep Degasser under vacuum conditions to produce uniform-sized mesopore and mixed-valent iron(II, III) clusters as reported in the literature [31,44]. Then, *in-situ* sonication of the heat-treated PCN-250(Fe) for 5 min under an inert atmosphere was done to achieve a more homogeneous particle size distribution to reach a uniform variation of the IL sheath thickness. Finally, the sonicated MOF, PCN-250(Fe)$_S$, which has a significantly lower average particle size, compared to the as-received one (see Table S3), was then mixed with $[P_{6,6,6,14}][DCA]$ via wet impregnation under air exclusion [45] to synthesize the MOFILS with a stoichiometric IL loading of 45 wt.%, which is slightly below the wetness limit of the material to maintain the powder state of the MOF. For this purpose, $[P_{6,6,6,14}][DCA]$ was removed from the glovebox and isothermally treated overnight in an oven at 80 °C to remove any remaining moisture. Afterward, 0.45 g of IL was dissolved in 30 mL acetone with constant stirring at 300 rpm for 1 h under ambient conditions and sealed with a septum to apply the gas bubbling step. The sealed mixture was placed inside an ice bath and bubbled with He for 45 min to remove any dissolved air. After 45 min, the mixture was heated up to room temperature and stirred for another 30 min at 300 rpm. To reach an approximate stoichiometric IL loading of 45 wt%, 0.55 g of MOF was loaded into a round bottom flask (RBF) inside an Ar-filled glovebox and was sealed with a septum to prevent any air exposure. Later, approximately 15 mL of acetone (deaerated by bubbling He) was added into the RBF containing pristine PCN-250(Fe) by an air-tight syringe, and the resulting mixture was sonicated for 5 min. Then, the He-bubbled IL-acetone mixture was carefully added to the septum-sealed RBF containing MOF by using a double-sided stainless-steel cannula under constant He flow to prevent air exposure. The double-sided cannula, having the exiting He flows from the IL-acetone mixture, was inserted through the septum of the RBF, and immediately after, another double-sided cannula was inserted through the septum to relieve the pressure build-up in the RBF. To transfer the IL-acetone mixture, one side of the cannula, which was connecting both flasks, was touched to the IL-acetone mixture, and with the help of the pressure difference, the whole mixture was transferred to the RBF. Upon the addition of the IL-acetone mixture, the cannulas were removed from the septum of the RBF in the order of first the one carrying the exiting He flow and then the one carrying the entering He flow. Instantly, the septum was sealed with vacuum grease and parafilm to prevent any leakage of air or moisture to the RBF. The obtained mixture containing dissolved IL in acetone and PCN-250(Fe) was left for stirring at 300 rpm overnight under room temperature to allow the deposition of IL molecules on the surface of the host material, MOF. Then, the mixture was connected to the Schlenk line for drying under vacuum. The resulting dried MOFILS in RBF was placed inside an Ar-filled glovebox and stored inside for further characterization and performance analysis.

3.3. Material characterization

3.3.1. X-ray fluorescence (XRF)

Approximate IL loading of the MOFILS was determined by X-ray fluorescence (XRF) spectroscopy technique with the help of a Bruker S8 Tiger spectrometer using an X-ray tube with a 4 kW Rh anode. Analyses were performed under helium atmosphere. The SpectraPlus Eval2 V2.2.454 software was used for the data interpretation.

3.3.2. Brunauer–Emmet–Teller (BET) analysis

Surface area determination of PCN-250(Fe)$_S$ and MOFILS were

performed by using a Micromeritics ASAP 2020 physisorption analyzer. Obtained N_2 physical adsorption and desorption data were analyzed both for surface area and pore volume. Prior to measurement, each sample was activated by degassing overnight at 240 °C for 12 h under vacuum. After the activation step, samples were cooled down to −196 °C by liquid nitrogen, and free space measurements were performed using He gas. Later, N_2 adsorption and desorption isotherms were obtained between a pressure range of 10^{-6} to 1 bar. Pressure steps between 0.05 and 0.3 bar were fitted to the BET equation, and t-plot analysis was conducted. Afterwards, obtained data were used to determine the surface area and pore volumes of each sample, respectively. Pore size distributions (PSD) were calculated by the Barrett–Joyner–Halenda (BJH) method.

3.3.3. Scanning electron microscopy (SEM)

SEM images of PCN-250(Fe), PCN-250(Fe)$_S$ and MOFILS were obtained by using a Zeiss Evo LS 15 scanning electron microscope. Analyses were conducted under vacuum with an accelerating voltage of 3 kV and a working distance of 3–3.3 mm. Images were taken with a magnification of 1 k, 10 k, and 20 k×. Prior to the analysis, PCN-250(Fe) samples were coated with gold to prevent any charging issues.

3.3.4. X-ray diffraction (XRD) spectroscopy

XRD spectroscopy of PCN-250(Fe), PCN-250(Fe)$_S$, and MOFILS were performed by using a Bruker D2 Phaser instrument with a Lynxeye detector. For the X-ray generator, Cu-Kα1 radiation source with a wavelength of 1.54060 Å was used at 30 kV voltage and 10 mA current to obtain XRD patterns. Slit size of 0.2 mm was used for the Lynxeye detector, whereas the diffraction data was collected between the 2θ range of 5-50° with a step size of 0.0204°. Deconvolution of the XRD pattern was made with XPSPeak version 4.1 software by using the Newton method for optimization of the designated peaks.

3.3.5. Thermal gravimetric analysis (TGA)

Thermal stability measurements were conducted by using a TA Instruments Q500 Thermogravimetric Analyzer with a platinum pan. For these measurements, approximately 10 mg of sample was used for both PCN-250(Fe)$_S$ and MOFILS. A constant temperature ramp rate of 5 °C/min was employed up to 240 °C, and the samples were treated isothermally for 9 h. Afterward, the temperature was increased to 700 °C at a ramp rate of 2 °C /min. All measurements were conducted under N_2 flow with the balance and purge gas rates of 40 and 60 mL/min, respectively. To analyze the thermal stability, the onset (T_{onset}) and derivative onset (T'_{onset}) temperatures were determined from the thermogravimetric (TG) and derivative TG curves (DTG), respectively. The T'_{onset} values were considered as the temperature point where the thermal decomposition initiated since T'_{onset} values generally overestimate the thermal decomposition temperatures [46].

3.3.6. Fourier-transform infrared (FTIR) spectroscopy

FTIR spectra of the filtrates were obtained by using a Bruker Vertex 80v IR spectrometer equipped with a platinum attenuated total reflection (ATR) accessory. Data were collected as an average of 256 scans for both the samples and their respective backgrounds. Measurements were performed at a spectral resolution of 2 cm^{-1} under atmospheric pressure between the wavelength range of 4000–400 cm^{-1}. Obtained data was compensated for atmospheric gasses, such as H_2O and CO_2, and corrected by using extended ATR modification with the help of OPUS software. Deconvolution of the obtained IR bands was conducted by using Fityk software using the Voigt function [47]. For air-sensitive PCN-250(Fe) samples, the FTIR spectra were obtained in a spectral range of 4000–400 cm^{-1} using an air-tight IR cell packed in an Ar-filled glove box. For these measurements, the pristine PCN-250(Fe), PCN-250(Fe)$_S$, and MOFILS were directly placed between the KBr windows of the cell, whereas the bulk ILs were first mixed with KBr powder (>99%, purchased from Merck) prior to packing the IR cell. Data analysis and corresponding baseline corrections were made by using OPUS software.

3.3.7. Transition electron microscopy (TEM) and energy dispersive spectroscopy (EDS)

The transmission electron microscopy (TEM) and energy dispersive spectroscopy (EDS) analysis were conducted using a Hitachi Hi-tech HF5000 TEM/STEM system, which was equipped with a third-order aberration corrector and a cold field emission gun (FEG) electron source. The analysis was performed at an accelerating voltage of 200 kV. Additionally, the microscope was fitted with an Oxford 100 mm^2 silicon drift twin energy-dispersive spectrometer that provided a solid angle of 1.7 sr.

3.3.8. Dynamic light scattering (DLS)

Dynamic light scattering analyses of the PCN-250(Fe)$_S$ sample were conducted with a Malvern Zetasizer Nano ZS by using a quartz cuvette. Scan numbers of 10 and run number of 3 were used for each sample with an analysis temperature of 25 °C. Z-Average sizes, obtained from intensity-based results, were reported.

3.3.9. Washing experiment

MOFILS (100 mg of powder samples) was washed with 4 mL of acetone at mild temperatures (approx. 50 °C) five-times. Later, washing filtrate was collected in a container for further analysis. Washed wet MOFILS samples were dried in an oven for 4 h at 105 ℃. Obtained powder products were used for further characterization.

3.4. High-pressure volumetric gas sorption measurements

Volumetric gas sorption measurements of the samples were performed for N_2 and O_2 by using a Quantachrome Instruments High-Pressure Volumetric Gas Adsorption Analyzer iSorb HP2. Approximately 0.4 g of sample was used for the measurements. Prior to the measurements, samples were degassed overnight for approximately 10 h while isothermally keeping them under vacuum at 240 °C at a vacuum pressure of 10^{-6} bar. After the activation step, the gas sorption isotherms for O_2 and N_2 were obtained at 10, 25, and 40 ℃ in a pressure range of 0.001–1 bar. Isotherms were collected by using iSorbHPwin High-Pressure Isotherms software.

Isotherm fittings were done by using IAST++ software [48]. Dual-Site Langmuir (DSL) model was used to fit the isotherms as given below,

$$DSL \rightarrow n(P) = q_1 \times \frac{k_1 \times P}{1 + k_1 \times P} + q_2 \times \frac{k_2 \times P}{1 + k_2 \times P}$$

where $n(P)$ is the adsorption quantity under equilibrium temperature, and P is the pressure. q_1 and q_2 represent the maximum adsorption capacity on sites #1 and #2, while k_1 and k_2 are the temperature-dependent equilibrium constants. Ideal Adsorbed Solution Theory (IAST) was used to predict the mixture gas adsorption based on the single-component gas adsorption data obtained from experimental measurements [49,50]. Mixture selectivity was calculated as the ratio of the adsorbed quantity of components in the mixture normalized by the ratio of mole fraction of the components in the bulk mixture.

4. Results and discussion

IL loading of the MOFILS was determined by XRF spectroscopy. The corresponding IL loading was calculated based on wt.% of P and Fe as approximately 47.8 wt.%, as given in Table S4. Since the pore limiting diameter of PCN-250(Fe) (approximately 4.3 Å as calculated by Zeo++ software [34]) is not large enough to allow the incorporation of [$P_{6,6,6,14}$][DCA] (having a comparably larger molecular size, approximately 27.1 Å as estimated from the DFT-optimized geometry), the prepared structure was expected to form a MOFILS, where the IL is surrounding the MOF particle as a sheath.

Figure S4 shows that no change was observed in the characteristic diffraction peaks of PCN-250(Fe)$_S$, indicating the integrity of the crystal structure was preserved, and structural stability was well-maintained after sonication. Figure S5(a) demonstrates that characteristic peaks of PCN-250(Fe)$_S$ were mostly preserved after the deposition of [$P_{6,6,6,14}$][DCA] layer, indicating that the crystalline structure was not distorted or collapsed during the synthesis of MOFILS. However, Figure S5(b) shows that some of the characteristic diffraction peaks are slightly blue-shifted in the MOFILS, accompanied by slight intensity changes that can be attributed to the layer formation and increasing electron density on the surface of the MOF cage, leading to a decrease in the dimensions of the MOF's crystallite size.

SEM images were obtained to investigate the surface morphologies of PCN-250(Fe)$_S$ and the corresponding MOFILS upon [$P_{6,6,6,14}$][DCA] coating. As supported by Fig. 1(a) and (b) and Figure S6, no alteration in crystal morphology was observed for pristine PCN-250(Fe) upon sonication. The brush-like structures observed in Fig. 1(c) and (d) were attributed to the IL sheath covering the surface of relatively large aggregated PCN-250(Fe)$_S$ crystals, indicating a distinctly different surface morphology for MOFILS. Images obtained at higher magnifications on smaller aggregates (by using TEM capable of imaging in secondary electron (SE), bright-field (BF), and dark-field (DF) modes simultaneously, as shown in Figure S7) indicate the absence of these brush-like structures but show the presence of a layer covering the surface of the MOFILS, as evidenced by the edge and surface features appearing rounded and smoothen out.

The BET and Langmuir surface areas of PCN-250(Fe)$_S$ and MOFILS are presented in Table S5 along with N_2 adsorption isotherms and pore volume distributions in Figure S8-S9. In the case of MOFILS, a dramatic decrease in the surface area was observed upon the deposition of [$P_{6,6,6,14}$][DCA]. Such a substantial decrease in the surface area can be considered as direct evidence for the successful deposition of the IL mostly onto the external surface of the MOF [20]. The pore volume of MOFILS could not be determined due to the inadequacy of data points associated with the poor solubility of the probe gas, N_2, in [$P_{6,6,6,14}$][DCA] at the measurement temperature. The [$P_{6,6,6,14}$][DCA] layer occupying the pore openings of PCN-250(Fe)$_S$ can obstruct the passage of N_2, leading to limitations in the determination of actual surface area and pore volume [25].

The recent results on IL/MOF composites, where the IL molecules are incorporated inside the MOF pores, show significant changes in the thermal stability limits of ILs associated with the presence of direct interactions [19,23,51]. Fig. 2(a) presents the T'_{onset} value of MOFILS (also tabulated in Table S6) as 307 ± 5 °C, nearly the same as that of bulk IL, [$P_{6,6,6,14}$][DCA], 305 ± 5 °C. These results indicate the absence of strong interactions between the IL molecules and the MOF in the MOFILS.

Fig. 2(b) and (c) and S10 compares the IR spectra of bulk IL, PCN-250 (Fe)$_S$, and MOFILS. It shows that the characteristic IR peaks of [$P_{6,6,6,14}$][DCA] located at approximately 2224, 2187, 2126 cm^{-1} corresponding to C≡N stretching vibration and 2957, 2926, 2854 cm^{-1} corresponding to C—H stretching of phosphonium cation [23,52] remain at the same position in the spectrum of the MOFILS, further confirming the absence of any direct interactions between IL and the MOF. Combining the results of TGA and IR analysis, we infer that the IL molecules are not preferentially located inside the MOF pores.

Molecular size of [$P_{6,6,6,14}$][DCA] (approximately 8.5 × 15.2 × 27.1 $Å^3$) is too large compared to the pore limiting diameter of the MOF (approximately 4.3 Å, as calculated by Zeo++ software [39]). This size difference suggests that the IL molecules can not diffuse into the pores. To confirm this inference, the samples were washed in acetone, a solvent with a molecular size (6.2 Å [53]) exceeding the pore aperture size of the MOF (4.3 Å), at 50 °C. IR spectra of the washed MOFILS (Figure S11) showed the disappearance of all IL-related features after washing, indicating the complete removal of the IL molecules. Because the solvent molecules are too large to be able to diffuse into the pores and wash out any IL molecules (if any), these results suggest that all the IL molecules were present on the external surface of the MOF particles. High-magnification TEM images obtained on the as-synthesized MOFILS complemented these results. A representative image given in Fig. 3(a) demonstrates the presence of a distinct layer with an average thickness of approximately 35 nm deposited on the external surface of PCN-250 (Fe)$_S$. The EDS analysis performed on these images shows that this distinct layer is characterized by the presence of phosphorus atoms (green), which are only present in the IL, and the absence of iron atoms (purple), which are only present in the MOF (Fig. 3(b) and (d)). Hence, we conclude that the distinct layer is associated with the IL molecules

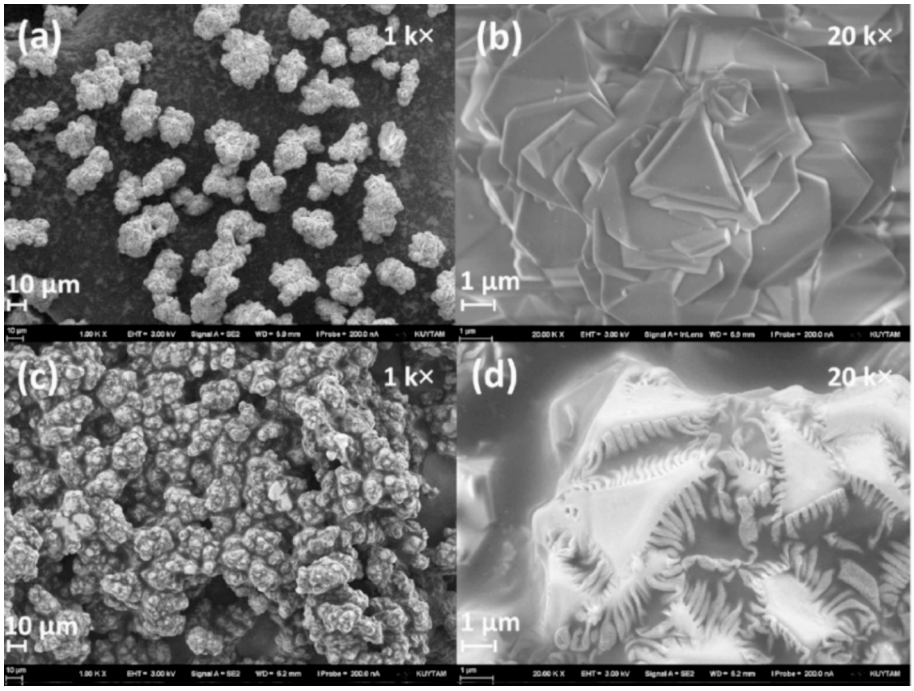


Fig. 1. SEM images of (a and b) PCN-250(Fe)$_S$ and (c and d) MOFILS acquired at magnifications of 1 k × (a and c) and 20 k × (b and d).

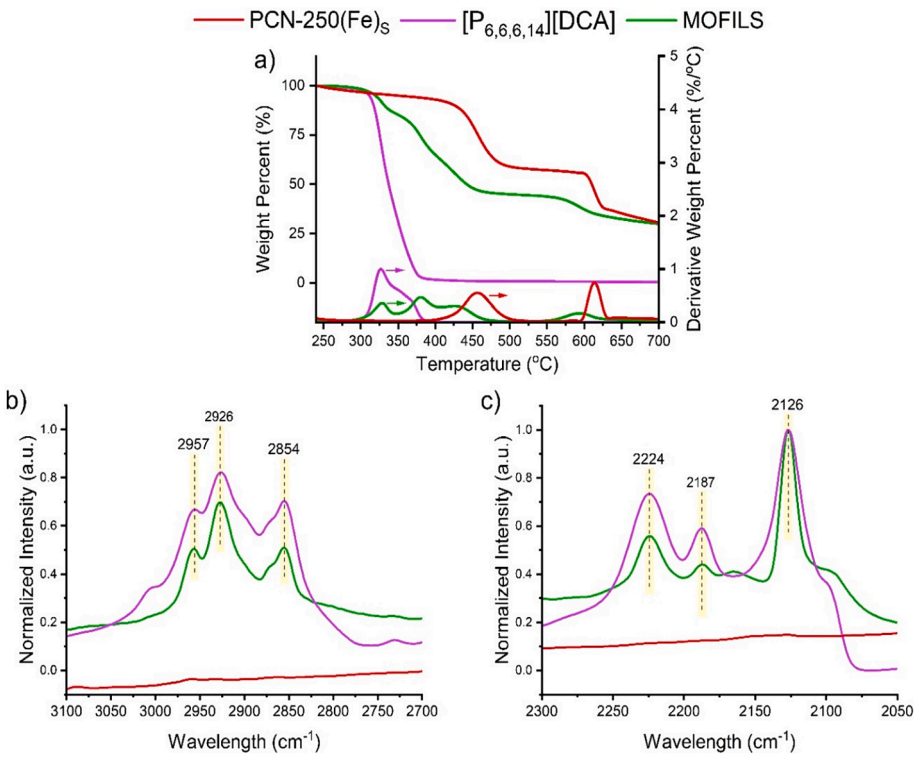


Fig. 2. (a) TGA and DTG curves of PCN-250(Fe)$_S$, bulk [$P_{6,6,6,14}$][DCA], and MOFILS. FTIR spectra of bulk [$P_{6,6,6,14}$][DCA], and MOFILS in the spectral ranges of (c) 3100–2700 cm^{-1}, (d) 2300–2050 cm^{-1}. PCN-250(Fe)$_S$ and MOFILS are isothermally treated at 240 ℃, and [$P_{6,6,6,14}$][DCA] is isothermally treated at 105 ℃ for 9 h prior to the start of the temperature ramp for the TGA measurements.

covering the external surface of the MOF particles as a sheath, confirming the MOFILS structure.

4.1. Gas adsorption and separation performance of MOFILS

Volumetric O_2 and N_2 gas adsorption isotherms of MOFILS and MOFs are compared in Fig. 4(a), with the related isotherm fitting parameters tabulated in Table S7. Data indicate that upon the IL deposition, volumetric O_2 adsorption of PCN-250(Fe)$_S$ increased by 2.7-times, from 8.1 to 21.5 cc/g, while the volumetric N_2 adsorption decreased by 5.5-times, from 4.5 to 0.8 cc/g, at 1 bar and 25 °C as demonstrated in Fig. 4(a). GCMC simulations were also performed to examine O_2 and N_2 adsorption in PCN-250(Fe)$_S$. The comparison between experimental and simulated O_2 and N_2 uptakes demonstrates a good agreement, as presented in Figure S12, for a pressure range of 0.1–1 bar at 25 °C. These changes in gas uptake values with the addition of the IL layer to form MOFILS are consistent with the DFT results demonstrating a distinct difference in the affinity of the IL towards O_2 and N_2.

The process of O_2 sorption in MOFILS involves two main stages: initial absorption on the IL sheath and subsequent adsorption on the PCN-250(Fe)$_S$ surface. Our washing experiment, outlined in Figure S11, confirmed that all IL molecules are located on the outer surface of the MOF. Consequently, the adsorption capacity of the MOF remains significantly intact, as the external surface area of the MOF particles has minimal contribution on its overall surface area. Therefore, it can be concluded that approximately 38% of the total O_2 sorption on MOFILS can be precisely attributed to O_2 adsorption on the MOF's internal surface, while the remaining is due to O_2 absorption on the IL sheath at 1 bar. Hence, we infer that the external IL sheath works as a smart O_2 selective filter for the MOF pores. These differences suggest a significant improvement in O_2/N_2 selectivity.

Cyclic adsorption measurements performed on MOFILS following the reactivation treatments, conducted at 10^{-6} bar and 240 °C for 12 h, confirmed the regenerability of O_2 sorption for 10 repetitive cycles, with an error range of less than 10% (see Figure S13). We also note that the mutual solubility of water and IL is crucial for the cyclic stability of the MOFILS as air contains water vapor. ILs containing $[P_{6,6,6,14}]^+$ cation are inherently hydrophobic because of the long aliphatic moieties attached to the cation core [54] and solubility of water in [$P_{6,6,6,14}$][DCA] was reported to be very low (0.029–0.033 in terms of mass fraction at 25 °C) [55–58]. Consequently, the hydrophobic IL sheath is anticipated to act as a barrier preventing the water sorption on the MOF, thereby helping to maintain its O_2 sorption capacity.

According to our DFT findings, the separation mechanism primarily arises from the IL sheath's strong attraction to O_2 molecules. In contrast, N_2 molecules are repelled due to their significantly lower binding energy with the IL. Consequently, the MOFILS exhibits approximately 14-times higher ideal O_2/N_2 selectivity (26.1) compared to PCN-250(Fe)$_S$ (1.8) at 1 bar and 25 °C, setting a new benchmark value among all previously reported MOFs for the same separation (Table S1). Separation performance of the MOFILS was much more remarkable at low pressures. Data indicate that the O_2/N_2 selectivity reaches 1393.1 (202.8) at 0.01 (0.1) bar, an approximately two orders of magnitude improvement compared to the corresponding selectivity obtained on the PCN-250(Fe). Moreover, the mixture separation performance of the MOFILS is investigated by using IAST, which is a widely used thermodynamic framework to predict mixed-gas adsorption isotherms based on the experimentally measured single-component gas isotherms. It has been shown to make accurate mixture adsorption data prediction on different MOFs [59–65] when there is no dynamic change on the structure of the adsorbent material [66,67]. Hence, the O_2/N_2:21/79 (v/v) mixture separation performance of MOFILS predicted by IAST showed a greater selectivity improvement compared to ideal selectivity. Fig. 4(b) shows that the MOFILS has a mixture selectivity of 382.1 at 1 bar significantly higher than that of any other MOFs at ambient conditions. For instance, at the same conditions, the $Co_2(OH)_2$(BBTA) [68] was reported to have a selectivity of 49. Moreover, at cryogenic conditions, the IAST predicted O_2/N_2 selectivities of Co-BDTriP [15] and Co-BTTri [15] were reported

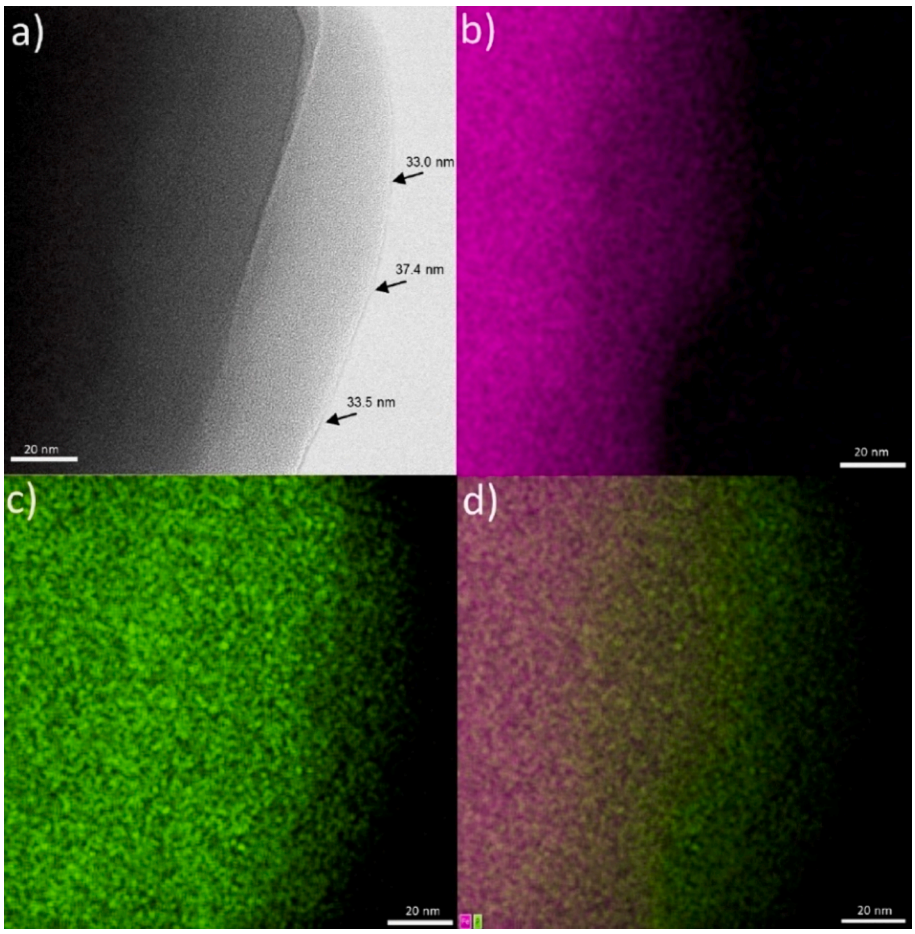


Fig. 3. TEM images of MOFILS at (a) 160 k× and (b-d) EDS map obtained on the same region resolving the MOF/IL sheath interface. Purple and green represent Fe and P, respectively.

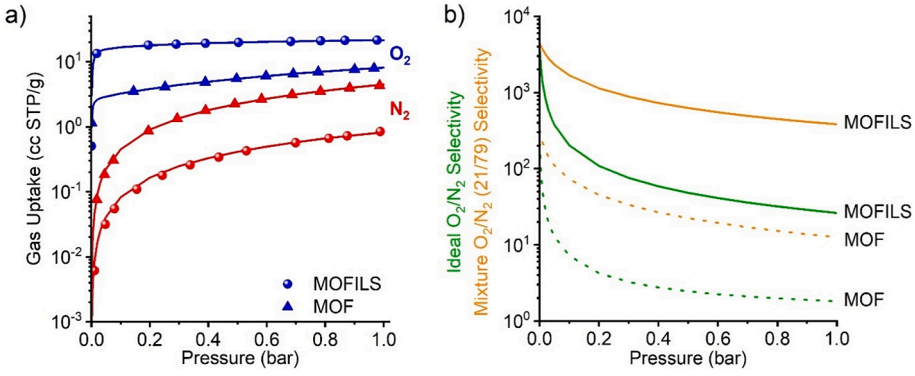


Fig. 4. (a) Single-component O_2 and N_2 gas adsorption isotherms of PCN-250(Fe)$_S$ and MOFILS at 25 ℃. Symbols represent the experimental data, and lines represent the fitted data. (b) Ideal O_2/N_2 selectivity and IAST-predicted O_2/N_2:21/79 mixture selectivity of the MOFILS and sonicated MOF at 25 ℃.

to be 105 and 41, respectively, at 1 bar and 195 K; however, these values drop significantly down to 40 and 13, respectively, at 243 K (Table S1).

To further validate the exceptional O_2/N_2 separation performance of the MOFILS from air, lab-scale breakthrough adsorption measurements were performed under a continuous flow of synthetic dry air at 5 mL/min O_2/N_2 (21/79, v/v) over a column packed with 450 mg of MOFILS, with 45 mL/min of He serving as a carrier gas at a temperature of 25 ℃ and 1 bar. The breakthrough time for each gas was determined by identifying the point at which C/C_0 reaches a value of 1%. As illustrated in Fig. 5, prior to the breakthrough, both O_2 and N_2 were adsorbed, resulting in no detection of either gas. Following the breakthrough, the concentration of N_2 increased initially at 55 s, followed by an increase in O_2 concentration at 125 s for PCN-250(Fe)$_S$, showing a retention of 70 s in between two gases, coinciding with the slightly preferential adsorption of the O_2 over N_2 of the PCN-250(Fe)$_S$. However, for the case of MOFILS, subsequent to the breakthrough, the concentration of N_2 increased initially at 150 s, followed by an increase in O_2 concentration at 430 s, indicating significantly higher preferential adsorption of the O_2 front, which can be attributed to the high affinity of the MOFILS towards O_2. Moreover, N_2 became oversaturated and was subsequently released, while O_2 remained in an adsorbed state during the time period of 150–430 s. The observed discrepancy in the breakthrough times of N_2

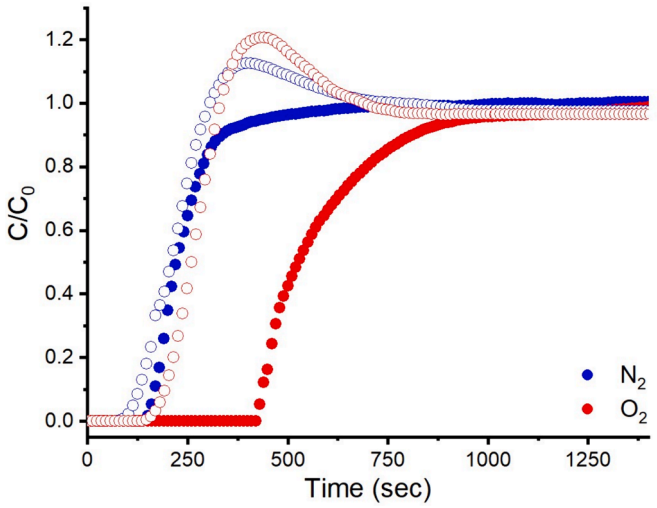


Fig. 5. Results of the adsorption column breakthrough measurement for PCN-250(Fe)$_S$ and MOFILS (450 mg) by flowing 5 ml/min dry air with 45 ml/min He as a carrier gas at 25 °C and 1 bar. The filled circles represent the MOFILS, and the empty circles represent the PCN-250(Fe)$_S$.

and O_2 indicates that MOFILS is capable of completely separating O_2 from N_2 for a duration of 280 s under the measurement conditions, leading to higher uptake amounts of O_2 than that of N_2 by replacing adsorbed N_2 over the adsorption site of MOFILS in dynamic conditions, corresponding to 9.5 cc/g high purity O_2 adsorption while it is only 0.5 cc/g of O_2 adsorption for PCN-250(Fe)$_S$. These experimental results obtained by the breakthrough measurements complement the high mixture selectivity of O_2/N_2 obtained by IAST predictions, reinforcing the promising potential of MOFILS for O_2 separation from air at ambient conditions.

5. Conclusion

A MOFILS, consisting of a phosphonium-based IL, [$P_{6,6,6,14}$][DCA], and an iron-based MOF with redox capability, PCN-250(Fe), was first computationally designed combining different computational tools, COSMO-RS calculations, DFT calculations, and GCMC simulations and then experimentally synthesized and tested for direct O_2 separation from air. Detailed characterization of the MOFILS confirmed the successful deposition of [$P_{6,6,6,14}$][DCA] molecules as a sheath, covering the PCN-250(Fe)$_S$ particles externally. The gas adsorption measurements demonstrated that MOFILS offers a remarkable ideal O_2/N_2 selectivity of 26.1 at 1 bar and 25 ℃, reaching a benchmark value among previously reported MOFs. Similarly, the IAST-calculated selectivity of MOFILS for O_2/N_2:21/79 mixture separation was calculated as 382.1 at 1 bar and 25 ℃, achieving a remarkable improvement for direct O_2 capture from the air compared to reported porous materials under these conditions. The high performance of the MOFILS in selectively separating O_2 from the air was also validated with a dynamic adsorption experiment, and the results demonstrated the highly preferential adsorption of O_2 over N_2. Furthermore, the successful regenerability of the MOFILS significantly increases its effective utilization for applications requiring repetitive cycles. Considering the unlimited number of IL-MOF pairs that can be used to make new MOFILS, our results highlight the significance of using computational methods as designing tools and the structural optimization of the synthesized MOFILS to achieve high-performance air separation.

CRediT authorship contribution statement

Ozce Durak: Writing – review & editing, Writing – original draft, Investigation, Formal analysis, Data curation. **Nitasha Habib:** Writing – review & editing, Writing – original draft, Investigation, Formal analysis, Data curation. **Hasan Can Gulbalkan:** Writing – review & editing, Writing – original draft, Investigation, Formal analysis, Data curation. **Ahmet Safa Aydogdu:** Writing – review & editing, Writing – original draft, Investigation, Formal analysis, Data curation. **Ray Ozdemir:** Writing – review & editing, Investigation, Formal analysis. **Seda Keskin:** Writing – review & editing, Writing – original draft, Supervision, Project administration, Methodology, Investigation, Funding acquisition. **Alper Uzun:** Writing – review & editing, Writing – original draft, Supervision, Project administration, Methodology, Investigation, Funding acquisition.

Declaration of competing interest

The authors declare that they have no known competing financial interests or personal relationships that could have appeared to influence the work reported in this paper.

Data availability

Data will be made available on request.

Acknowledgment

S.K. acknowledges ERC-2017-Starting Grant. This research has received funding from the European Research Council (ERC) under the European Union's Horizon 2020 research and innovation program (ERC-2017-Starting Grant, grant agreement no. 756489-COSMOS). A.U. thanks the Fulbright Türkiye's Visiting Scholar Program, Türkiye; the Koç University Visiting Scholar Program, Türkiye, and the Scientific and Technological Research Council of Türkiye (TUBITAK) 2219 Program, Türkiye. The authors gratefully acknowledge the support of Koç University TÜPRAŞ Energy Center (KUTEM)and we thank Dr. Barış Yağcı, Gülsu Şimşek, and Amir Motallebzadeh of Koç University Surface Science and Technology Center (KUYTAM) with providing help on SEM, XRF, BET, and XRD along with Keisuke Igarashi, Hiroaki Matsumoto, and N2STAR for providing help with TEM/EDS. Finally, authors thank Dr. Zeynep Pınar Haşlak for the fruitful discussion on DFT calculations. The authors acknowledge Tuğser Yılmaz and Asst. Prof. Umut Aydemir of the Koç University Boron and Advanced Materials Application and Research Center (KUBAM) for their help in XRD measurements.

Appendix A. Supplementary data

Supplementary data to this article can be found online at https://doi.org/10.1016/j.cej.2024.152608.

References

[1] G.A. Ospina-Tascón, L.E. Calderón-Tapia, A.F. García, V. Zarama, F. Gómez-Álvarez, T. Álvarez-Saa, S. Pardo-Otálvaro, D.F. Bautista-Rincón, M.P. Vargas, J. L. Aldana-Díaz, Effect of high-flow oxygen therapy vs conventional oxygen therapy on invasive mechanical ventilation and clinical recovery in patients with severe COVID-19: a randomized clinical trial, J. Am. Med. Assoc. 326 (21) (2021) 2161–2171.
[2] K. Walter, Mechanical Ventilation, J. Am. Med. Assoc. 326 (14) (2021) 1452.
[3] M.E. Boot-Handford, J.C. Abanades, E.J. Anthony, M.J. Blunt, S. Brandani, N. Mac Dowell, J.R. Fernández, M.-C. Ferrari, R. Gross, J.P. Hallett, R.S. Haszeldine, P. Heptonstall, A. Lyngfelt, Z. Makuch, E. Mangano, R.T.J. Porter, M. Pourkashanian, G.T. Rochelle, N. Shah, J.G. Yao, P.S. Fennell, Carbon capture and storage update, Energ. Environ. Sci. 7 (1) (2014) 130–189.
[4] A. Atkinson, S. Barnett, R.J. Gorte, J. Irvine, A.J. McEvoy, M. Mogensen, S. C. Singhal, J. Vohs, Advanced anodes for high-temperature fuel cells, Nat. Mater. 3 (1) (2004) 17–27.
[5] C. Liu, J. Qian, Y. Ye, H. Zhou, C.-J. Sun, C. Sheehan, Z. Zhang, G. Wan, Y.-S. Liu, J. Guo, Oxygen evolution reaction over catalytic single-site Co in a well-defined brookite TiO2 nanorod surface, Nat. Catal. 4 (1) (2021) 36–45.
[6] R. Águas, A. Mahdi, R. Shretta, P. Horby, M. Landray, L. White, Potential health and economic impacts of dexamethasone treatment for patients with COVID-19, Nat. Commun. 12 (1) (2021) 915.

[7] O. World Health, Oxygen sources and distribution for COVID-19 treatment centres: interim guidance, 4 April 2020, World Health Organization, Geneva, 2020.

[8] X. Yang, Y. Yu, J. Xu, H. Shu, J. Xia, H. Liu, Y. Wu, L. Zhang, Z. Yu, M. Fang, T. Yu, Y. Wang, S. Pan, X. Zou, S. Yuan, Y. Shang, Clinical course and outcomes of critically ill patients with SARS-CoV-2 pneumonia in Wuhan, China: a single-centered, retrospective, observational study, Lancet Respir. Med. 8 (5) (2020) 475–481.

[9] S.W. Chai, M.V. Kothare, S. Sircar, Rapid Pressure Swing Adsorption for Reduction of Bed Size Factor of a Medical Oxygen Concentrator, Ind. Eng. Chem. Res. 50 (14) (2011) 8703–8710.

[10] K. Adil, Y. Belmabkhout, R.S. Pillai, A. Cadiau, P.M. Bhatt, A.H. Assen, G. Maurin, M. Eddaoudi, Gas/vapour separation using ultra-microporous metal–organic frameworks: insights into the structure/separation relationship, Chem. Soc. Rev. 46 (11) (2017) 3402–3430.

[11] J.-R. Li, R.J. Kuppler, H.-C. Zhou, Selective gas adsorption and separation in metal–organic frameworks, Chem. Soc. Rev. 38 (5) (2009) 1477–1504.

[12] J.W. Yoon, H. Chang, S.-J. Lee, Y.K. Hwang, D.-Y. Hong, S.-K. Lee, J.S. Lee, S. Jang, T.-U. Yoon, K. Kwac, Selective nitrogen capture by porous hybrid materials containing accessible transition metal ion sites, Nat. Mater. 16 (5) (2017) 526–531.

[13] L.J. Murray, M. Dinca, J. Yano, S. Chavan, S. Bordiga, C.M. Brown, J.R. Long, Highly-selective and reversible O_2 binding in Cr_3(1,3,5-benzenetricarboxylate)$_2$, J. Am. Chem. Soc. 132 (23) (2010) 7856–7857.

[14] E.D. Bloch, W.L. Queen, M.R. Hudson, J.A. Mason, D.J. Xiao, L.J. Murray, R. Flacau, C.M. Brown, J.R. Long, Hydrogen Storage and Selective, Reversible O_2 Adsorption in a Metal-Organic Framework with Open Chromium(II) Sites, Angew. Chem. Int. Ed. 55 (30) (2016) 8605–8609.

[15] D.J. Xiao, M.I. Gonzalez, L.E. Darago, K.D. Vogiatzis, E. Haldoupis, L. Gagliardi, J. R. Long, Selective, tunable O_2 binding in cobalt (II)–triazolate/pyrazolate metal–organic frameworks, J. Am. Chem. Soc. 138 (22) (2016) 7161–7170.

[16] D.A. Reed, D.J. Xiao, H.Z.H. Jiang, K. Chakarawet, J. Oktawiec, J.R. Long, Biomimetic O_2 adsorption in an iron metal–organic framework for air separation, Chem. Sci. 11 (6) (2020) 1698–1702.

[17] Y. Li, R.T. Yang, Gas Adsorption and Storage in Metal−Organic Framework MOF-177, Langmuir 23 (26) (2007) 12937–12944.

[18] E.D. Bloch, L.J. Murray, W.L. Queen, S. Chavan, S.N. Maximoff, J.P. Bigi, R. Krishna, V.K. Peterson, F. Grandjean, G.J. Long, B. Smit, S. Bordiga, C.M. Brown, J.R. Long, Selective Binding of O_2 over N_2 in a Redox-Active Metal–Organic Framework with Open Iron(II) Coordination Sites, J. Am. Chem. Soc. 133 (37) (2011) 14814–14822.

[19] F.P. Kinik, A. Uzun, S. Keskin, Ionic liquid/metal–organic framework composites: from synthesis to applications, Chem. Sus. Chem 10 (14) (2017) 2842–2863.

[20] O. Durak, M. Zeeshan, N. Habib, H.C. Gulbalkan, A.A.A.M. Alsuhile, H.P. Caglayan, S.F. Kurtoğlu-Öztulum, Y. Zhao, Z.P. Haslak, A. Uzun, S. Keskin, Composites of porous materials with ionic liquids: Synthesis, characterization, applications, and beyond, Microporous Mesoporous Mater. 332 (2022) 111703.

[21] M. Zeeshan, V. Nozari, M.B. Yagci, T. Isık, U. Unal, V. Ortalan, S. Keskin, A. Uzun, Core-Shell Type Ionic Liquid/Metal Organic Framework Composite: An Exceptionally High CO_2/CH_4 Selectivity, J. Am. Chem. Soc. 140 (32) (2018) 10113–10116.

[22] J. Yang, M. Tong, G. Han, M. Chang, T. Yan, Y. Ying, Q. Yang, D. Liu, Solubility-Boosted Molecular Sieving-Based Separation for Purification of Acetylene in Core-Shell IL@MOF Composites, Adv. Funct. Mater. (2023) 2213743.

[23] S. Hussain, H. Dong, Y. Zhang, G. Zhan, S. Zeng, H. Duan, X. Zhang, Impregnation of 1-n-Butyl-3-methylimidazolium Dicyanide [BMIM][DCA] into ZIF-8 as a Versatile Sorbent for Efficient and Selective Separation of CO_2, Ind. Eng. Chem. Res. 61 (1) (2021) 706–715.

[24] M. Zeeshan, V. Nozari, M.B. Yagci, T. Isık, U. Unal, V. Ortalan, S. Keskin, A. Uzun, Core–shell type ionic liquid/metal organic framework composite: an exceptionally high CO_2/CH_4 selectivity, J. Am. Chem. Soc. 140 (32) (2018) 10113–10116.

[25] Y. Lan, T. Yan, M. Tong, C. Zhong, Large-scale computational assembly of ionic liquid/MOF composites: synergistic effect in the wire-tube conformation for efficient CO_2/CH_4 separation, J. Mater. Chem. A 7 (20) (2019) 12556–12564.

[26] K. Huang, Y.-T. Wu, X.-B. Hu, Effect of alkalinity on absorption capacity and selectivity of SO_2 and H_2S over CO_2: Substituted benzoate-based ionic liquids as the study platform, Chem. Eng. J. 297 (2016) 265–276.

[27] Y.G. Chung, E. Haldoupis, B.J. Bucior, M. Haranczyk, S. Lee, H. Zhang, K. D. Vogiatzis, M. Milisavljevic, S. Ling, J.S. Camp, Advances, updates, and analytics for the computation-ready, experimental metal–organic framework database: CoRE MOF 2019, J. Chem. Eng. Data 64 (12) (2019) 5985–5998.

[28] H. Daglar, I. Erucar, S. Keskin, Exploring the performance limits of MOF/polymer MMMs for O_2/N_2 separation using computational screening, J. Membr. Sci. 618 (2021) 118555.

[29] Y. Yan, Z. Shi, H. Li, L. Li, X. Yang, S. Li, H. Liang, Z. Qiao, Machine learning and in-silico screening of metal–organic frameworks for O_2/N_2 dynamic adsorption and separation, Chem. Eng. J. 427 (2022) 131604.

[30] I.B. Orhan, H. Daglar, S. Keskin, T.C. Le, R. Babarao, Prediction of O_2/N_2 Selectivity in Metal-Organic Frameworks via High-Throughput Computational Screening and Machine Learning, ACS Appl. Mater. Interfaces 14 (1) (2021) 736–749.

[31] H.F. Drake, G.S. Day, S.W. Vali, Z. Xiao, S. Banerjee, J. Li, E.A. Joseph, J. E. Kuszynski, Z.T. Perry, A. Kirchon, O.K. Ozdemir, P.A. Lindahl, H.-C. Zhou, The thermally induced decarboxylation mechanism of a mixed-oxidation state carboxylate-based iron metal–organic framework, Chem. Commun. 55 (85) (2019) 12769–12772.

[32] Y.S. Sistla, A. Khanna, Validation and prediction of the temperature-dependent Henry's constant for CO_2–ionic liquid systems using the conductor-like screening model for realistic solvation (COSMO-RS), J. Chem. Eng. Data 56 (11) (2011) 4045–4060.

[33] K. Paduszyński, An overview of the performance of the COSMO-RS approach in predicting the activity coefficients of molecular solutes in ionic liquids and derived properties at infinite dilution, PCCP 19 (19) (2017) 11835–11850.

[34] T.F. Willems, C.H. Rycroft, M. Kazi, J.C. Meza, M. Haranczyk, Algorithms and tools for high-throughput geometry-based analysis of crystalline porous materials, Microporous Mesoporous Mater. 149 (1) (2012) 134–141.

[35] A.D. Becke, Density-functional thermochemistry. I. The effect of the exchange-only gradient correction, J. Chem. Phys. 96 (3) (1992) 2155–2160.

[36] C. Lee, W. Yang, R.G. Parr, Development of the Colle-Salvetti correlation-energy formula into a functional of the electron density, Phys. Rev. B 37 (2) (1988) 785.

[37] S. Grimme, J. Antony, S. Ehrlich, H. Krieg, A consistent and accurate ab initio parametrization of density functional dispersion correction (DFT-D) for the 94 elements H-Pu, J. Chem. Phys. 132 (15) (2010) 154104.

[38] A.E. Reed, R.B. Weinstock, F. Weinhold, Natural population analysis, J. Chem. Phys. 83 (2) (1985) 735–746.

[39] S.F. Boys, F. Bernardi, The calculation of small molecular interactions by the differences of separate total energies. Some Procedures with Reduced Errors, Molecular Physics 19 (4) (1970) 553–566.

[40] A. Meunier, B. Lévy, G. Berthier, Electron correlation and basis effects in the theory of hydrogen bonds: The mixed dimer ammonia-water, Theor. Chim. Acta 29 (1973) 49–55.

[41] J. Zhang, S.H. Chai, Z.A. Qiao, S.M. Mahurin, J. Chen, Y. Fang, S. Wan, K. Nelson, P. Zhang, S. Dai, Porous liquids: a promising class of media for gas separation, Angew. Chem. 127 (3) (2015) 946–950.

[42] M. Zeeshan, H.C. Gulbalkan, O. Durak, Z.P. Haslak, U. Unal, S. Keskin, A. Uzun, An Integrated Computational-Experimental Hierarchical Approach for the Rational Design of an IL/UiO-66 Composite Offering Infinite CO_2 Selectivity, Adv. Funct. Mater. 32 (35) (2022) 2204149.

[43] A. Koutsianos, R. Pallach, L. Frentzel-Beyme, C. Das, M. Paulus, C. Sternemann, S. Henke, Breathing porous liquids based on responsive metal-organic framework particles, Nat. Commun. 14 (1) (2023) 4200.

[44] H.F. Drake, Z. Xiao, G.S. Day, S.W. Vali, W. Chen, Q. Wang, Y. Huang, T.-H. Yan, J. E. Kuszynski, P.A. Lindahl, Thermal decarboxylation for the generation of hierarchical porosity in isostructural metal–organic frameworks containing open metal sites, Mater. Adv. 2 (16) (2021) 5487–5493.

[45] A.H. Mason, A. Motta, A. Das, Q. Ma, M.J. Bedzyk, Y. Kratish, T.J. Marks, Rapid atom-efficient polyolefin plastics hydrogenolysis mediated by a well-defined single-site electrophilic/cationic organo-zirconium catalyst, Nat. Commun. 13 (1) (2022) 7187.

[46] K. Jin, X. Huang, L. Pang, J. Li, A. Appel, S. Wherland, [Cu(i)(bpp)]BF_4: the first extended coordination network prepared solvothermally in an ionic liquid solvent, Chem. Commun. 23 (2002) 2872–2873.

[47] M. Wojdyr, Fityk: a general-purpose peak fitting program, J. Appl. Cryst. 43 (5–1) (2010) 1126–1128.

[48] S. Lee, J.H. Lee, J. Kim, User-friendly graphical user interface software for ideal adsorbed solution theory calculations, Korean J. Chem. Eng. 35 (2018) 214–221.

[49] A.L. Myers, J.M. Prausnitz, Thermodynamics of mixed-gas adsorption, AIChE J 11 (1) (1965) 121–127.

[50] K.S. Walton, D.S. Sholl, Predicting multicomponent adsorption: 50 years of the ideal adsorbed solution theory, AIChE J 61 (9) (2015) 2757–2762.

[51] M. Zeeshan, V. Nozari, S. Keskin, A. Uzun, Structural factors determining thermal stability limits of ionic liquid/MOF composites: imidazolium ionic liquids combined with CuBTC and ZIF-8, Ind. Eng. Chem. Res. 58 (31) (2019) 14124–14138.

[52] Y. Dong, M. Gong, F.U. Shah, A. Laaksonen, R. An, X. Ji, Phosphonium-based ionic liquid significantly enhances SERS of cytochrome *c* on TiO_2 nanotube arrays, ACS Appl. Mater. Interfaces 14 (23) (2022) 27456–27465.

[53] A.B. Nadykto, F. Yu, Uptake of neutral polar vapor molecules by charged clusters/particles: Enhancement due to dipole-charge interaction, J. Geophys. Res. Atmos. 108 (D23) (2003).

[54] K.A. Kurnia, M.V. Quental, L.M. Santos, M.G. Freire, J.A. Coutinho, Mutual solubilities between water and non-aromatic sulfonium-, ammonium-and phosphonium-hydrophobic ionic liquids, PCCP 17 (6) (2015) 4569–4577.

[55] C.M. Neves, P.J. Carvalho, M.G. Freire, J.A. Coutinho, Thermophysical properties of pure and water-saturated tetradecyltrihexylphosphonium-based ionic liquids, J. Chem. Thermodyn. 43 (6) (2011) 948–957.

[56] M.G. Freire, P.J. Carvalho, R.L. Gardas, L.M. Santos, I.M. Marrucho, J.A. Coutinho, Solubility of water in tetradecyltrihexylphosphonium-based ionic liquids, J. Chem. Eng. Data 53 (10) (2008) 2378–2382.

[57] J. Marták, Š. Schlosser, Extraction of lactic acid by phosphonium ionic liquids, Sep. Purif. Technol. 57 (3) (2007) 483–494.

[58] I. Rodriguez-Escontrela, I. Rodriguez-Palmeiro, O. Rodriguez, A. Arce, A. Soto, Liquid–liquid–liquid equilibria for water+[P_{66614}][DCA]+dodecane ternary system, Fluid Phase Equilib. 405 (2015) 124–131.

[59] Z. Niu, X. Cui, T. Pham, G. Verma, P.C. Lan, C. Shan, H. Xing, K.A. Forrest, S. Suepaul, B. Space, A MOF-based Ultra-Strong Acetylene Nano-trap for Highly Efficient C_2H_2/CO_2 Separation, Angew. Chem. 133 (10) (2021) 5343–5348.

[60] G.-D. Wang, Y.-Z. Li, W.-J. Shi, L. Hou, Y.-Y. Wang, Z. Zhu, Active Sites Decorated Nonpolar Pore-Based MOF for One-step Acquisition of C_2H_4 and Recovery of C_3H_6, Angew. Chem. (2023) e202311654.

[61] Y. Sun, S. Hu, J. Yan, T. Ji, L. Liu, M. Wu, X. Guo, Y. Liu, Oriented Ultrathin π-complexation MOF Membrane for Ethylene/Ethane and Flue Gas Separations, Angew. Chem. (2023) e202311336.

[62] Y. Wang, H. Jin, Q. Ma, K. Mo, H. Mao, A. Feldhoff, X. Cao, Y. Li, F. Pan, Z. Jiang, A MOF glass membrane for gas separation, Angew. Chem. 132 (11) (2020) 4395–4399.
[63] G.D. Wang, R. Krishna, Y.Z. Li, W.J. Shi, L. Hou, Y.Y. Wang, Z. Zhu, Boosting Ethane/Ethylene Separation by MOFs through the Amino-Functionalization of Pores, Angew. Chem. Int. Ed. 61 (48) (2022) e202213015.
[64] Y. Jiang, J. Hu, L. Wang, W. Sun, N. Xu, R. Krishna, S. Duttwyler, X. Cui, H. Xing, Y. Zhang, Comprehensive Pore Tuning in an Ultrastable Fluorinated Anion Cross-Linked Cage-Like MOF for Simultaneous Benchmark Propyne Recovery and Propylene Purification, Angew. Chem. Int. Ed. 61 (18) (2022) e202200947.
[65] S.M. Wang, X.T. Mu, H.R. Liu, S.T. Zheng, Q.Y. Yang, Pore-Structure Control in Metal-Organic Frameworks (MOFs) for Capture of the Greenhouse Gas SF_6 with Record Separation, Angew. Chem. 134 (33) (2022) e202207066.
[66] N.F. Cessford, N.A. Seaton, T. Düren, Evaluation of ideal adsorbed solution theory as a tool for the design of metal–organic framework materials, Ind. Eng. Chem. Res. 51 (13) (2012) 4911–4921.
[67] R. Babarao, Z. Hu, J. Jiang, S. Chempath, S.I. Sandler, Storage and separation of CO_2 and CH_4 in silicalite, C_{168} schwarzite, and IRMOF-1: a comparative study from Monte Carlo simulation, Langmuir 23 (2) (2007) 659–666.
[68] A.S. Rosen, M.R. Mian, T. Islamoglu, H. Chen, O.K. Farha, J.M. Notestein, R. Q. Snurr, Tuning the redox activity of metal–organic frameworks for enhanced, selective O_2 binding: Design rules and ambient temperature O_2 chemisorption in a cobalt–triazolate framework, J. Am. Chem. Soc. 142 (9) (2020) 4317–4328.